Self-Assembled Gallium Sulde (GaS) HeterostructuresEnabling Ecient Water Splitting and Selective AmmoniaSensing

ADVANCED FUNCTIONAL MATERIALS
www.afm-journal.de

Self-Assembled Gallium Sulfide (GaS) Heterostructures Enabling Efficient Water Splitting and Selective Ammonia Sensing

Danil W. Boukhvalov, Gianluca D'Olimpio, Tsotne Dadiani, Jyayasi Sharma, Ashraf Abdelrahman Assadig Elameen, Stefano Zenone, Marcin Rosmus, Bekir Gürbulak, Emir Çepni, Eduard Llobet, Elena Magnano, Federica Bondino, Songül Duman,* and Antonio Politano**

Herein, a comprehensive validation of the catalytic and sensing capabilities of gallium sulfide (GaS). This study focuses on the self-assembled heterostructure formed by GaS with its native oxide, revealing novel insights into the crucial role of defects, strain, and surface oxide phases in optimizing the behavior of 2D materials for catalytic and sensing applications. Although the energy barrier for water dissociation on pristine GaS surfaces is prohibitive (+419.3 kJ mol^{-1}), surface sulfur vacancies considerably reduce this barrier, transforming defective GaS (GaS$_x$) into an efficient catalyst for the hydrogen evolution reaction (HER) in alkaline media. Water dissociation is energetically favorable at room temperature on GaS$_{0.96}$ surfaces (−147.6 kJ mol^{-1}). Correspondingly, the differential free energy for HER on GaS$_{0.96}$ in an alkaline medium is found to be −1.56 eV for the hydroxyl adsorption step and +1.28 eV for the desorption step, while all reaction steps are exothermic for its implementation as a catalyst for oxygen evolution reaction (OER). These theoretical models and surface-science experiments confirm that exposure of GaS surfaces to ambient conditions leads to the inevitable formation of a self-assembled nanoscale (≈3 nm thick) oxide skin. This native oxide layer stabilizes the surface and, moreover, it also significantly enhances its catalytic and sensing properties by providing additional active sites and improving charge transfer dynamics. The exceptional sensitivity (response of 18% at T = 150 °C) and selectivity for detecting ammonia (NH$_3$) are attributed to both its high affinity for chemisorption and the significant charge-transfer interactions that enhance the sensor response.

1. Introduction

The advent of 2D materials has had a groundbreaking impact on materials science[1–4] and, particularly surface science.[5–8] The unique surface properties of 2D materials make them uniquely suited for applications in which surface chemistry plays a decisive role in their functionality and efficiency.[9–11] As a matter of fact, owing to their atomic thickness, 2D materials provide a large surface area, maximizing the number of active sites.[12,13] Consequently, 2D materials can be engineered for applications based on surface chemical reactions such as gas sensing and photoelectrochemistry.[14] In gas sensing, changes in the electrical conductivity of 2D materials upon gas adsorption onto their surfaces allow for the rapid, selective, and ultrasensitive detection of toxic gases.[15] Similarly, in electrochemistry, the tunable electronic properties afforded by the thickness-dependent bandgap energy in 2D semiconductors[16,17] enable precise control over the redox potentials, facilitating efficient charge transfer.

D. W. Boukhvalov
College of Science
Institute of Materials Physics and Chemistry
Nanjing Forestry University
Nanjing 210037, P. R. China
E-mail: danil@njfu.edu.cn

The ORCID identification number(s) for the author(s) of this article can be found under https://doi.org/10.1002/adfm.202507388

DOI: 10.1002/adfm.202507388

G. D'Olimpio, T. Dadiani, A. A. A. Elameen, S. Zenone, A. Politano
Department of Physical and Chemical Sciences
University of L'Aquila
via Vetoio, L'Aquila (AQ) 67100, Italy
E-mail: antonio.politano@univaq.it

J. Sharma, E. Llobet
Universitat Rovira i Virgili
MINOS, Avda. Països Catalans, 26, Tarragona 43007, Spain

A. A. A. Elameen, S. Zenone
Department of Applied Science and Technology
Polytechnic University of Turin
Corso Castelfidardo, 39, Turin 10129, Italy

M. Rosmus
National Synchrotron Radiation Center SOLARIS
Jagiellonian University
Czerwone Maki 98, Krakow PL-30392, Poland

Among 2D semiconductors, group III-VI metal chalcogenides (MX), where M is Ga or In, and X is a chalcogen atom (S, Se, Te),[18–20] provide several advantages, including superior tunability of the bandgap, high optical absorption in the visible range of the electromagnetic spectrum, and high carrier mobility.[21] While the majority of III-VI MX compounds have indirect band gaps in their bulk form and a direct band gap in the monolayer regime,[22–24] GaS uniquely exhibits an indirect bandgap in both the bulk and monolayer.[25,26] Generally, indirect bandgap materials allow prolonged carrier lifetimes compared to their direct-gap counterparts, considering that the momentum conservation rule requires the involvement of a phonon to facilitate electron transitions between the valence and conduction bands, which typically results in slower recombination rates.[27,28]

Beyond its potential in optoelectronics,[18,29–32] GaS is a promising candidate for gas sensing[31,33] and (photo)electrochemical (PEC) devices.[34–36] Indirect bandgap materials are often advantageous for gas sensing applications.[37] Prolonged carrier lifetimes allow for extended interaction times between the target gas molecules and the sensor material, potentially leading to higher sensitivity and selectivity in gas detection. In addition, an indirect bandgap could lead to a more efficient utilization of the solar spectrum[38] in PEC. Furthermore, the small energy difference between the indirect and direct band gaps (only 0.52 eV for bulk GaS[39]) implies that GaS can effectively mimic the behavior of a direct bandgap semiconductor under illumination or at elevated temperatures. This dual behavior naturally enhances the versatility of GaS in PEC applications, in which both light absorption and efficient charge separation and transport are crucial for high performance.[40]

Moreover, the ability to tune electronic properties through external stimuli, such as light,[41] allows the development of smart electrochemical devices that can adapt their behavior in response to changing environmental conditions. This adaptability can be particularly useful in sensing applications such as environmental monitoring and industrial process control.

B. Gürbulak
Department of Physics
Faculty of Sciences
Atatürk University
Erzurum 25240, Türkiye

E. Çepni
Department of Electrical and Electronics Engineering
Faculty of Engineering
Atatürk University
Erzurum 25240, Türkiye

E. Magnano, F. Bondino
Consiglio Nazionale delle Ricerche (CNR) - Istituto Officina dei Materiali (IOM)
Area Science Park S.S. 14 km 163.5, Trieste 34149, Italy

S. Duman
Basic Sciences Department
Faculty of Sciences
Erzurum Technical University
Erzurum 25050, Türkiye
E-mail: songul.duman@erzurum.edu.tr

D. W. Boukhvalov
Institute of Physics and Technology
Satbayev University
Ibragimov str. 11, Almaty 050032, Kazakhstan

One of the challenges associated with the use of 2D materials in such devices is their stability under ambient conditions. Density functional theory (DFT) calculations have shown that defect-free MX monolayers exhibit excellent oxidation resistance when exposed to O_2.[42] However, this resistance can be degraded in the presence of single chalcogen vacancies with small barriers of only 0.26–0.36 eV for the chemisorption of a single O_2 molecule.[42] Oxidation can often be detrimental to the functionality of devices owing to the degradation of their electronic and structural properties.[43] However, the self-assembled formation of a native metal oxide layer can also provide opportunities to improve the overall efficiency, particularly in catalysis and environmental sensing applications. As a matter of fact, oxygen vacancies can act as active sites in catalytic processes[44] or for gas adsorption,[45] thereby enhancing both the catalytic activity and detectability of gases at lower concentrations. Furthermore, the nanoscale oxide skin is passivated; hence, it represents an inherently stable interface for chemical reactions.[46] Additionally, controlled oxidation can be used to tailor the bandgap[47–49] to optimize the activity of PEC cells by improving their matching with the solar spectrum, thereby enhancing the overall efficiency of solar-to-fuel conversion. Therefore, it is critical to overcome the challenges related to controlling the oxidation process by gaining a detailed understanding of the oxidation mechanisms and developing techniques to control it at the atomic level, including information on the (*i*) kinetics of the oxidation process, (*ii*) stability of the oxide skin under the operational conditions, and (*iii*) reversibility of the oxidation process.

In light of these considerations, studies on the ambient stability of GaS, particularly on how its surface is transformed during processes such as air exposure or exfoliation, are essential. Such studies could provide insights into the best way to handle and exploit the oxidation process to enhance functionality in applications, such as electrocatalysis and environmental sensing. These insights are pivotal for developing robust and efficient PEC devices and gas sensors. Previously, GaS nanosheet-based PEC devices showed superb responsivities of 1.8, 4.6, and 6.8 mA W^{-1} in 1 M H_2SO_4 at 0.8 V versus the reversible hydrogen electrode (RHE), 1 M Na_2SO_4 at 0.9 V versus RHE, and 6.8 mA W^{-1} in 1 M KOH at 1.1 V versus RHE under 275 nm illumination with an intensity of 1.3 mW cm^{-2}.[50] However, the observed PEC activity was attributed to the intrinsically high surface area of the 2D GaS layers, which were also assumed to be inert despite the evident fingerprints of surface oxidation emerging from the analysis of both the microscopic images and core-level spectra.[51] Although early implementations of GaS in PEC devices have shown promise, the lack of detailed insights into the key reaction steps in the catalytic processes hinders further optimization. Addressing these gaps can fully realize the potential of GaS in innovative technologies that contribute to cleaner energy and improved environmental monitoring.

In this study, we investigated the catalytic and sensing capabilities of self-assembled heterostructures formed by GaS and its native oxides. Through a combination of experiments and DFT calculations, we demonstrated that surface vacancies and native oxide layers play crucial roles in enhancing the efficiency of GaS for PEC applications and gas sensing at room temperature. Our findings show that the introduction of surface S vacancies significantly reduces the energy barriers for the HER and OER,

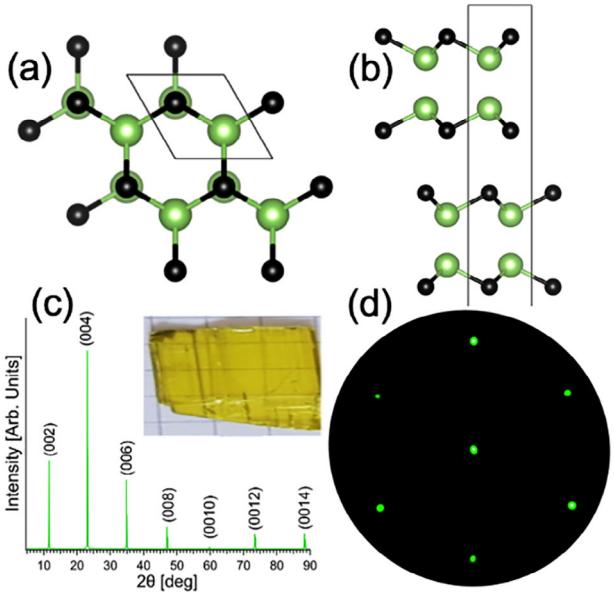

Figure 1. a) Top and b) side views of the atomic structure of GaS. Green and black balls denote Ga and S atoms, respectively, in the figure. c) XRD pattern of the grown single-crystal GaS, whose photograph is shown in the inset. d) LEED pattern.

making GaS an efficient catalyst. Additionally, the native oxide layer stabilizes the GaS surface under operational conditions and provides additional active sites (O vacancies), thereby improving the charge transfer dynamics and boosting the catalytic and sensing performances. Specifically, the heterostructure exhibited remarkable sensitivity and selectivity toward ammonia, which was attributed to the strong chemisorption and charge transfer interactions. These insights pave the way for the exploitation of GaS-based heterostructures in sustainable energy solutions and environmental monitoring.

2. Results and Discussion

2.1. Atomic Structure

Gallium sulfide crystallizes from the melt as hexagonal β-GaS with space group no. 19 ($P6_3/mmc$,[52–54] **Figure 1**a,b). The β-GaS phase is particularly stable and can undergo a reversible polymorphic transition to ϵ-GaS only at pressures exceeding 3 GPa.[55] The primitive unit cell of the hexagonal β phase had a lattice parameter of $a = 3.596$ Å and $c = 15.550$ Å, as confirmed by X-ray diffraction (XRD) (Figure 1c), which is in agreement with previous investigations.[56–59] The low-energy electron diffraction (LEED) pattern of the as-cleaved surfaces revealed sharp, intense spots forming a distinct hexagonal pattern, indicative of surface crystallinity (Figure 1d). The unit cell of the hexagonal GaS phase is composed of two S-Ga-Ga-S quadruple layers,[52,60] with prevailing covalent intralayer bonding and negligible ionic contribution,[61,62] whereas weak interlayer van der Waals forces regulate the interlayer cohesion along the optical c-axis.[32,63]

To gain a deeper understanding of the electronic properties contributing to the catalytic and sensing capabilities of GaS, angle-resolved photoemission spectroscopy (ARPES) was conducted. The synchrotron-based ARPES data presented in **Figure 2** provide a comprehensive overview of the band structure. The valence band maximum is located at the center of the Brillouin zone, and the topmost valence band maximum exhibits a parabolic shape with a flat region at the peak, resembling a pudding mold dispersion.[31] This unique electronic structure results in a high density of states at the valence band edge, facilitating enhanced charge carrier separation and transport. These characteristics are beneficial for PEC applications because they enable more efficient light absorption and charge transport,[64] thereby improving the performance of devices such as water-splitting photoelectrodes. Additionally, the presence of flat bands around the valence band maximum can be beneficial for the adsorption of analytes[65] and, consequently, for gas sensing applications.[66] In fact, an increased density of states can lead to stronger interactions with gas molecules,[67] potentially improving the sensitivity and selectivity of GaS-based gas sensors.

2.2. Surface Chemical Reactivity and Ambient Stability

First-principles calculations were performed to assess the chemical stability and catalytic properties of GaS. For this purpose, we used a slab of four layers constructed from 3 × 3 GaS supercells (**Figure 3**). First, the stability of the lattice was evaluated by calculating the energy required for the formation of S vacancies, which was as high as +366.6 kJ mol^{-1}. Therefore, the number of S vacancies can be considered small, even after exfoliation. However, considering their potential influence on the catalytic activity of GaS, the effect of S vacancies was considered in our theoretical model.

Thermal annealing in controlled atmospheres is a versatile strategy for modulating the concentration and nature of point defects in GaS. By carefully selecting the ambient conditions during the annealing process, it is possible to either promote or suppress the formation of sulfur vacancies. For instance, annealing under a sulfur-rich atmosphere, typically achieved using H_2S or elemental sulfur vapor, can increase the chemical potential of sulfur, thereby favoring the reincorporation of sulfur atoms into the vacancy sites. This thermodynamically driven process leads to partial re-sulfurization of the surface and a consequent reduction in the vacancy concentration. Conversely, annealing in oxygen-rich environments, such as ambient air or diluted O_2, at elevated temperatures promotes the oxidation of surface sulfur atoms and their desorption in the form of SO_2 or other volatile species. This oxidation-driven mechanism increases the sulfur vacancy concentration and initiates the formation of an amorphous Ga_2O_3 skin on the GaS surface.

In addition to thermal treatments, chemical doping offers an additional means to stabilize or destabilize specific defect configurations. The introduction of aliovalent dopants can shift the Fermi level locally and alter the defect formation energy landscape. This can lead to the preferential stabilization of neutral or charged vacancies, depending on the doping element and chemical environment.

In the present work, while we do not claim to exert fine control over the defect population, we observed that intrinsic defects, expected to form preferentially at the grain boundaries or step edges, are essential for the functionality of the material, and their

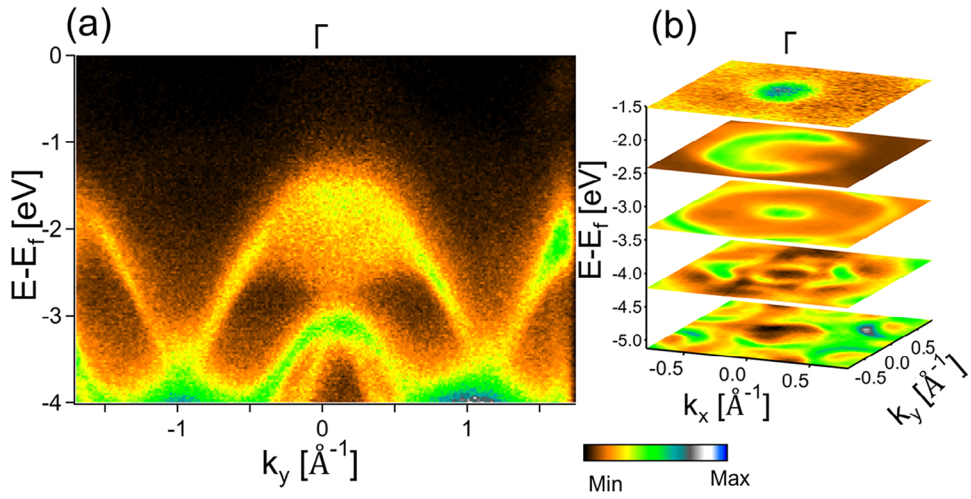

Figure 2. a) Electronic band structure of the GaS crystal at $h\nu = 100$ eV and $T = 80$ K and b) isoenergy contours around the center of the Brillouin zone.

tunability through annealing or doping represents a promising direction for future optimizations.

We modeled the physisorption and subsequent decomposition of oxygen and water molecules on defect-free and defective GaS. At room temperature, both physisorption ($\Delta G = -129.9$ kJ mol^{-1}) and decomposition ($\Delta H = -104.5$ kJ mol^{-1}) of O_2 (Figure 3a,b) are exothermic processes, even on defect-free surfaces.

To explore the mechanisms underlying the formation of S vacancies when GaS interacts with oxygen (Figure 3c), we conducted a detailed analysis of the energy pathways involved. The $GaS + x\,O_2 \rightarrow GaS_{1-x} + x\,SO_2$ process initially has an energy cost of +205.5 kJ mol^{-1}, indicating that S atom removal is energetically unfavorable (Figure 3c). This suggests that S vacancies are unlikely to form in the early stages of the interaction between the GaS surface and an oxidative environment, thus ensuring surface stability. However, as oxidation advanced, ultimately leading to an oxygenated surface layer (Ga_2S_2O, Figure 3c), the process became exothermic, releasing 37.6 kJ mol^{-1}, making further oxidation energetically favorable. The presence of S vacancies further lowered the energy barrier, as indicated in **Table 1**. Although the additional adsorption of oxygen on Ga_2S_2O remains energetically costly (+57.1 kJ mol^{-1} for physisorption and +123.2 kJ mol^{-1} for decomposition), the formation of S vacancies with SO_2 release becomes exothermic, with an energy gain of −96.7 kJ mol^{-1}, promoting the formation of a stable Ga_2O_3-like layer.

In contrast, water (H_2O) adsorption at room temperature on the GaS substrate is energetically favorable ($\Delta G = -63.4$ kJ mol^{-1}), occurring primarily through physisorption, unlike the decomposition observed for molecular oxygen. The adsorption of water on Ga_2S_2O at room temperature is metastable, with a corresponding ΔG of +5.9 kJ mol^{-1}. The subsequent decomposition of water molecules is energetically favorable for S-vacancy sites and oxidized surfaces. However, the high energy cost of the decomposition of water molecules on

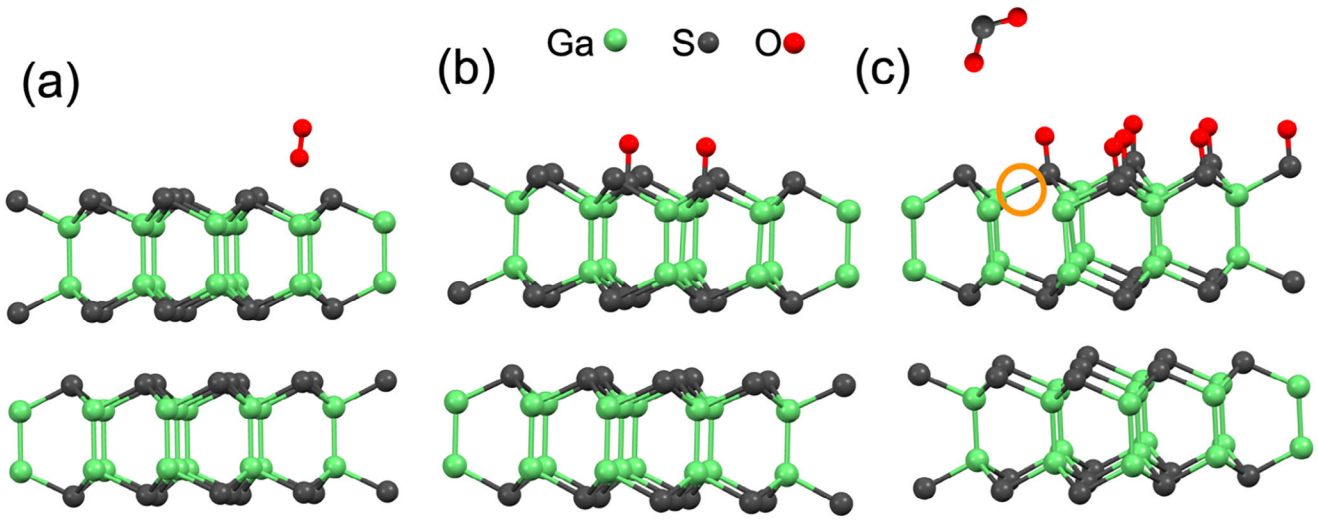

Figure 3. Optimized atomic structures for a) physisorption and b) decomposition of oxygen molecules on the GaS substrate. Panel c) depicts the formation of sulfur vacancies (orange circles) on the oxidized surface of GaS with the simultaneous formation of SO_2.

Table 1. Differential enthalpy (ΔH) and Gibbs free energy (ΔG) of physisorption and decomposition of oxygen and water molecules on the GaS surface with ($GaS_{0.96}$) and without sulfur vacancies and an oxygen layer (Ga_2S_2O). The values in parentheses represent the differential oxidation enthalpies for the entire surface.

Specie	Substrate	Physisorption		Decomposition ΔH [kJ mol^{-1}]
		ΔH [kJ mol^{-1}]	ΔG [kJ mol^{-1}]	
O_2	GaS	−141.4	−129.9	−104.5 (-37.6)
	$GaS_{0.96}$	−176.4	−164.9	−243.1 (-44.2)
	Ga_2S_2O	+45.6	+57.1	+123.2
H_2O	GaS	−96.5	−63.4	+419.3
	$GaS_{0.96}$	−147.9	−114.8	−147.6
	Ga_2S_2O	−27.2	+5.9	−85.0

defect-free GaS surfaces (+419.3 kJ mol^{-1}) suggests the effectiveness of the liquid-phase exfoliation of GaS in water. This result can be extended to other solvents used for liquid-phase exfoliation, in agreement with the literature results for GaS-based functional inks,[68] which usually exhibit almost defect-free flakes.

To assess the stability of GaS in oxidative environments, including air, we conducted controlled experiments using X-ray photoelectron spectroscopy (XPS) with synchrotron radiation to exploit its superior surface sensitivity owing to its ability to use lower photon energies,[69] which are crucial for detecting subtle changes in surface chemistry[70] compared with standard XPS with lab-scale sources.

The as-cleaved GaS surface exhibited distinct single doublets in both Ga-3d and S-2p spectra, with Ga-$3_{5/2}$ and S-$2p_{3/2}$ components at a binding energy (BE) of 19.6 eV (**Figure 4**a) and 161.9 eV (Figure 4b), respectively. Additionally, a weak spectral feature corresponding to Ga-3s was observed at $BE = 160.3$ eV (Figure 4b).

The GaS surface was then exposed to up to 10^6 L (1 L = 10^{-6} Torr s^{-1}) of O_2, and the evolution of the core-level spectra was monitored. Neither the Ga-3d nor S-2p core levels showed new components (Figure 4), proving that even prolonged exposure to O_2 under vacuum conditions is insufficient to induce oxidation of the GaS nanosheets, in agreement with the high energy barrier for oxidation estimated by our model (+205.5 kJ mol^{-1}). Similarly, the oxidation robustness was valid even for short-term (i.e., 1–10 min) air exposure (**Figure 5**). For storage in the air extended up to one hour, the segregation of metallic Ga from the bulk led to the emergence of a Ga(0) component in Ga-3d core levels with a BE of 19.4 eV for the Ga-$3d_{5/2}$ component (Figure 5). Its spectral weight increased from 15% of the total Ga-3d area in the spectrum after one hour in the air to 22% after one day in the air. Ga(0) species are prone to oxidation and hydroxylation, as indicated by the oxide and hydroxide components observed after one month of air storage, as indicated by the Ga-$3d_{5/2}$ components at BEs of 20.5 and 21.7 eV, respectively. The feature at BE = 20.5 eV associated with oxygenated and oxidized GaS can be attributed to both partial and complete etching of the surface sublayer of S, with the formation of S vacancies, corresponding to the formation of GaS_xO (in the early stages of oxidation) and Ga_2O_3 surface phases (at saturation) for long-term exposure to oxidative environments. It should be noted that the presence of $Ga(OH)_3$ can be attributed to the decomposition of water molecules from the ambient air humidity on such S vacancies. Correspondingly, the S-2p core levels showed a new component emerging

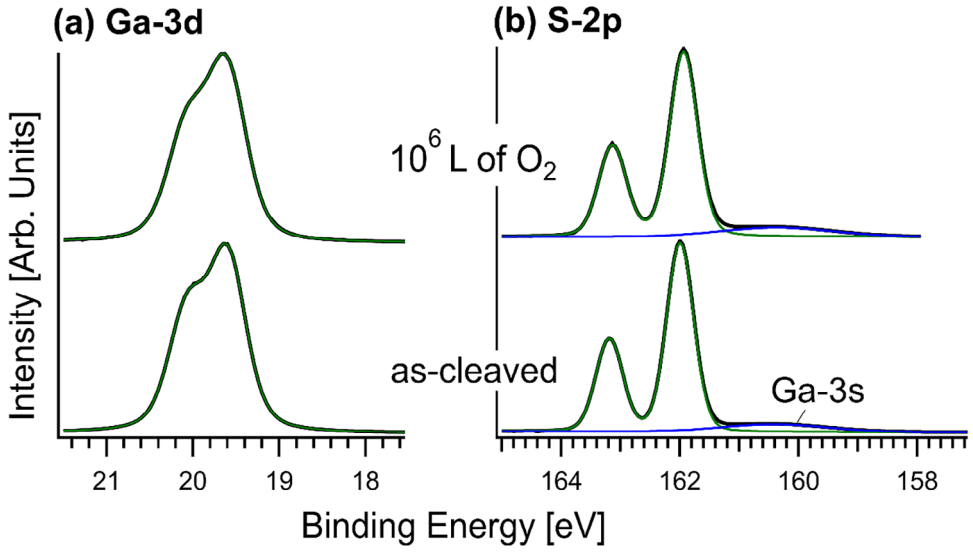

Figure 4. a) Ga-3d and b) S-2p core levels of the as-cleaved GaS surface and its response to 10^6 L O_2 exposure. The photon energy was set to 657 eV. The spectra were normalized to the maximum intensity.

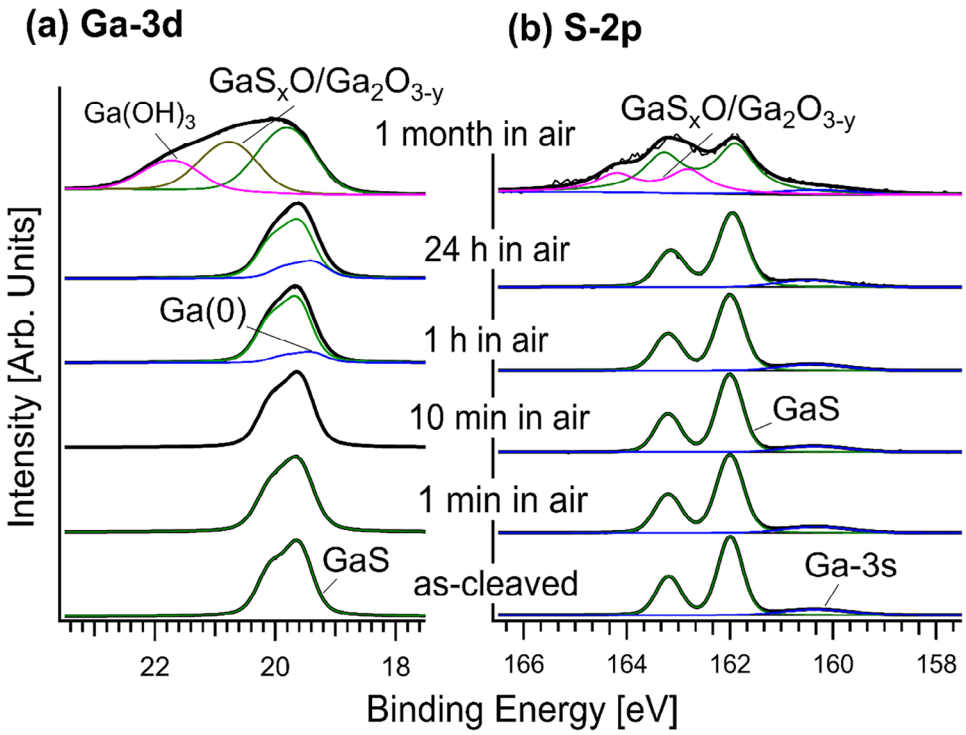

Figure 5. a) Ga-3d and b) S-2p core levels of as-cleaved GaS in air after 1, 10 min, 2, 24 h, and 1 month. The photon energy was 657 eV, and each spectrum was normalized to its maximum height.

associated with the corresponding GaS_xO at a BE of 162.8 eV for the $J = 3/2$ component.

Remarkably, from the analysis shown in Figure 5, it is evident that the oxidation of GaS is self-limiting, which is in agreement with our theoretical model. Similar conclusions can be drawn from the corresponding survey and O-1s spectra presented in Figures S1 and S2, (Supporting Information) respectively. Thus, it can be inferred that the self-assembled heterostructure formed by GaS and its native oxide exhibits chemical stability. This information is crucial for optimizing the stability and performance of GaS in applications such as catalysis[71] and gas sensing,[72] where maintaining chemical activity under operational conditions[73] without poisoning the active sites is essential.

Additionally, it is worth noting the absence of Ga_2S_3 in the core-level spectra of GaS exposed to oxidative environments, in contrast to the oxidation path observed for the parental compounds InSe and GaSe,[74] in which In_2Se_3 and Ga_2Se_3 intermediates play key roles. To check the possibility of the formation of Ga_2S_3, we calculated the differential enthalpy for the following reaction:

$$12GaS + 3O_2 \rightarrow 4Ga_2S_3 + 2Ga_2O_3 \quad (1)$$

This reaction is exothermic, with an energy gain of 6.9 kJ mol^{-1}. This value is one order lower than the energy gain from oxygen decomposition, even in non-defective GaS (104.5 kJ mol^{-1}), and five times lower than the energy gain for the formation of the Ga_2S_2O phase (37.6 kJ mol^{-1}). Thus, the reaction pathway leading to GaS oxidation avoids the formation of intermediate, less stable sulfide phases, with the direct formation of the more stable Ga_2O_3. The absence of Ga_2S_3-related spectral features in the core levels of the aged GaS surfaces, as shown in Figure 5, is consistent with previous cathodoluminescence investigations of the thermal oxidation of GaS single crystals, which exhibited only lines corresponding to GaS and Ga_2O_3.[75]

Transmission electron microscopy (TEM) analysis provided crucial insights into the morphology and crystalline structure of GaS nanoflakes after extended exposure to ambient conditions, assessing both the structural integrity and formation of oxide layers on the GaS nanosheets. The low-magnification TEM image (**Figure 6a**) provides an overview of the GaS nanosheets and demonstrates their sizes and distribution. The high-resolution TEM (HR-TEM) image (Figure 6b) was focused on a specific area to reveal its atomic structure. The d-spacing values for the highlighted fringes of the crystallographic planes (Figure 6c) were determined to be 0.381 and 0.255 nm for the (004) and (006) planes, respectively. HR-TEM analysis of the amorphous native oxide layer with a thickness of 3.2 nm, formed upon exposure to air, did not reveal any crystalline lattices (Figure 6e). The absence of diffraction rings in the corresponding small-area electron diffraction (SAED) pattern further indicates the emergence of an amorphous oxide skin (Figure 6f). In contrast, the SAED pattern of the basal plane shows well-arranged diffraction spots indicated by the Miller indices (ICDD PDF number: 00-001-0478) in a hexagonal pattern (Figure 6d), suggesting a high crystalline quality. The hexagonal structure and d-spacing values were in good agreement with the XRD data for the GaS bulk sample, as shown in Figure 1c. This stark difference in the diffraction patterns emphasizes the formation of an amorphous oxide layer in the edge regions of the GaS surface exposed to air, whereas the

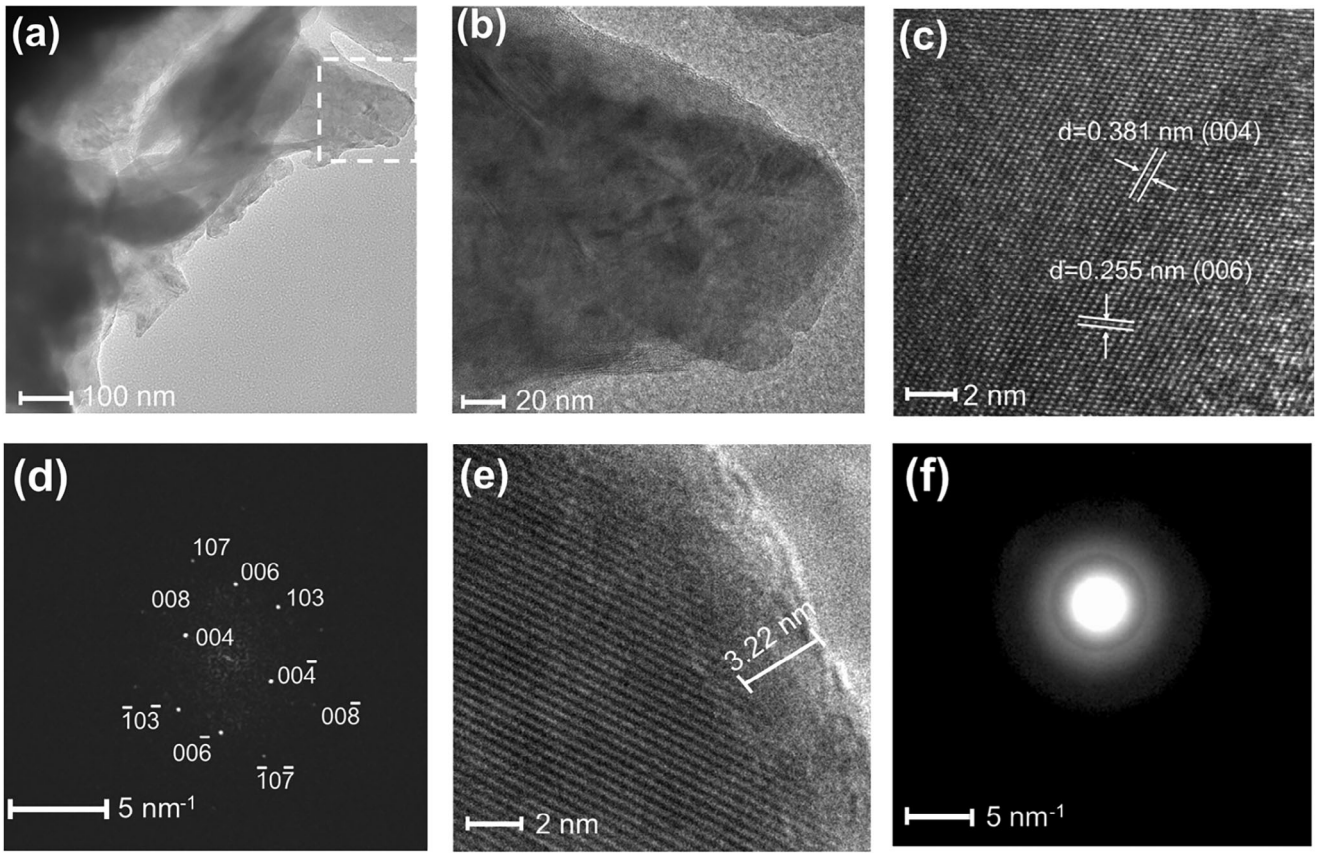

Figure 6. a) Low-magnification TEM image of GaS nanosheets after three months in air. b) HR-TEM image of the area marked in panel (a). c) HRTEM image and d) SAED pattern of the crystalline area in panel (b). e) HRTEM image and f) SAED pattern of the amorphous area in panel (b).

basal plane retained its high crystallinity even after liquid-phase exfoliation.

2.3. Electrochemistry

Experimental studies on GaS nanosheets prepared through liquid exfoliation validated GaS as an effective catalyst for the HER in acidic environments, specifically in 0.5 M sulfuric acid (H_2SO_4).[68] Specifically, GaS nanosheets exhibited Tafel slopes ranging between 85 and 106 mV per decade,[68] which are lower than the typical ≈120 mV per decade observed for molybdenum disulfide (MoS_2). This suggests that GaS may have a different rate-determining step, potentially enhancing its catalytic efficiency at higher current densities. The overpotential necessary to reach a current density of 1 mA/cm^2 (onset potential) for GaS nanosheets varied depending on their lateral size, with values approximately 0.62 V for 450 nm, 0.53 V for 280 nm, and 0.48 V for 180 nm nanosheets.[68] At a higher potential of 0.6 V, the observed current densities were 0.6, 1.2, and 1.9 mA cm^{-2} for the 450, 280, and 180 nm nanosheets, respectively.[68] The catalytic activity of the GaS nanosheets was mainly attributed to their 2D structure,[68] owing to their intrinsically superior surface area, which improved the overall catalytic performance. Similar conclusions have been reported for the PEC activity of 2D GaS-based PEC devices in previous studies.[50] Moreover, it has been claimed that the contribution of any gallium oxide (Ga_2O_3) phase to the observed catalytic activity should be minimal, as oxides reside mostly near the edges of GaS nanosheets and at the step sites.[68]

However, this picture should be revised based on our detailed simulations of the HER in acidic and alkaline media and the OER in acidic media. To enhance the comprehensiveness of the studies, we also accounted for the presence of residual sulfur, as indicated in a recent investigation on GaS.[51] We also examined the effects of substrate-induced distortions and structural deformations on the catalytic properties of surface oxide layers. Because the hexagonal structure of the GaS layer (see Figure 1a) can also be represented by a tetragonal structure, we modeled the in-plane tetragonal distortions in the Ga_2O_3-based slabs. Simulations of the HER in acidic media demonstrated that hydrogen adsorption on defect-free GaS was an endothermic process with an energy cost of 1.58 eV (**Figure** 7a) because there were no dangling bonds in the surface layer. In contrast, the adsorption of hydrogen near S vacancy sites corresponding to dangling bonds in the surface layer is an exothermic process with an energy gain of 0.92 eV. However, the subsequent hydrogen desorption with the formation of an H_2 molecule requires the same amount of energy owing to the restoration of the dangling bond on the surface. The calculated energies for the six Ga_2O_3-based compounds indicate that only tetragonalized Ga_2O_3 (denoted as "t-Ga_2O_3") and $Ga_2O_{2.98}$ are suitable for the HER in acidic media. The adsorption

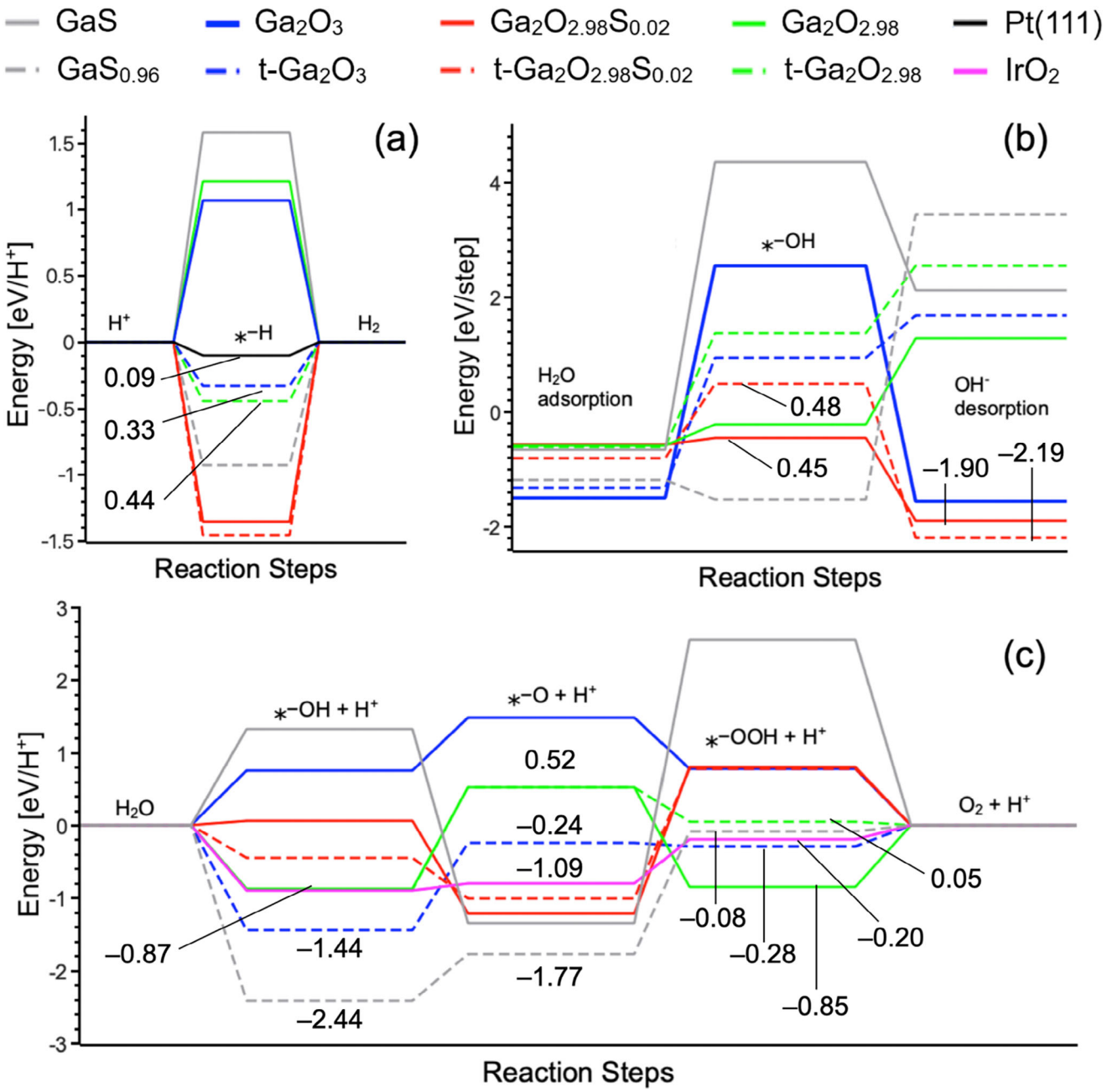

Figure 7. Free energies per step of the HER in a) acidic and b) alkaline media and c) OER in acidic media for GaS, GaS_x ($x = 0.96$), and Ga_2O_3-based substrates. The substrates are marked with asterisks. The reference values for Pt(111) for the HER and Ir_2O for the OER have been reported. The numerical values of the free energies are reported for the most promising substrates.

of hydrogen on these substrates is an exothermic process, and the formation of H_2 molecules requires relatively moderate energy costs (0.44 and 0.33 eV, respectively). These relatively moderate adsorption energy magnitudes correspond to the interplay between the energy cost of defect formation and the energy gain from the restriction of bonds by structural distortions. These values approach that of Pt (0.09 eV, Figure 7a).

Next, we modeled the HER in an alkaline medium. For this reaction, a combination of low-energy water decomposition and OH- desorption is essential. The results shown in Figure 7b demonstrate that the first step of the HER is energetically costly (4.34 eV) for non-defective GaS, and the second step is energetically costly for $GaS_{0.96}$ (3.44 eV). In contrast, for S-doped nontetragonalized Ga_2O_3, all HER steps in alkaline media are exothermic. The tetragonalization of $Ga_2O_{2.98}$ $S_{0.02}$ transforms the second step (water decomposition) into an endothermic reaction. However, the energy cost of this step is moderate (0.48 eV). Thus, based on the results of our simulations, we can conclude that the experimentally observed catalytic performance of GaS-based systems can be attributed to the formation of Ga_2O_3 phases.

We also modeled the OER in an acidic medium (Figure 7c). This reaction over the non-defective GaS substrate corresponds to two endothermic steps with relatively high energy costs (1.32 and 2.55 eV). The introduction of S vacancies in GaS renders all steps exothermic. However, the high energy gain of the first two steps over the $GaS_{0.96}$ substrate (−2.42 and −1.77 eV) corresponds to the irreversible oxidation of the catalytic substrate. Thus, the formation of a Ga_2O_3-based surface phase after several OER steps can be concluded. The OER simulation over six Ga_2O_3-based substrates showed that tetragonalized oxygen-rich Ga_2O_3 and both $Ga_2O_{2.98}$-based substrates displayed energetics similar to those of IrO_2 (Figure 7c), which is considered the best catalyst for the OER.[76,77] Sulfur-doped Ga_2O_3-based systems are also good candidates for the OER because the two initial steps of the reaction are exothermic with a moderate energy gain, and the final step corresponds to a moderate energy cost of ≈0.8 eV. Thus, the results of our simulations demonstrate the efficiency of the Ga_2O_3-like slabs formed on the surface of GaS for the OER under acidic conditions.

2.4. Gas Sensing

The self-assembled heterostructure formed by the van der Waals semiconductor GaS and its native oxide could also represent an ideal platform for gas sensing. Recent experimental studies have shown that GaS nanosheets exhibit high sensitivity to NH_3, with an enhanced photoresponse in an NH_3 environment, which is attributed to the increased carrier density resulting from NH_3 adsorption.[31]

Theoretical calculations also suggest that vacancy defects in GaS monolayers significantly decrease the adsorption energies of toxic gases such as SO_2, HCN, and NH_3,[78] making defect-engineered GaS highly suitable for gas-sensing applications. However, these studies did not consider the inevitable oxidation of GaS surfaces. Moreover, only the values of the differential enthalpies of adsorption were reported in this study. At room temperature, the differential free energy of adsorption of all the analytes at the defect sites was higher than that of oxygen and water. The calculated probability of adsorption on the defect sites at room temperature suggests that oxygen molecules occupy these sites in GaS in an oxidative environment.

The surface oxide skin also provides active sites for reactions with analyte gases. This aspect is even more relevant for Ga_2O_3, considering that Ga_2O_3-based films and nanostructures represent a state-of-the-art platform for gas sensing.[79–82] Therefore, we performed simulations of the adsorption of various molecules present in the ambient atmosphere (oxygen, water, hydrogen, carbon monoxide, and carbon dioxide) and those, which can also be considered pollutants (ammonia, nitrogen and sulfur dioxides, and hydrogen cyanide). The simultaneous calculation of the adsorption of various analytes on the considered substrates enables the consideration of competition between different molecules for active surface sites at given temperatures. Similar to the case of catalysis, we considered several types of Ga_2O_3-based substrates: nondistorted and tetragonalized slabs of non-defective Ga_2O_3, slabs with substitutional S impurities ($Ga_2O_{2.98}$ $S_{0.02}$), and O vacancies ($Ga_2O_{2.98}$). The atomic structures of the nontetragonalized substrates are shown in **Figure 8a–c**.

Table 2 reports the differential adsorption enthalpies and Gibbs free energies at room temperature and 150 °C to highlight how thermal activation modifies the relative stability of adsorbed species and enables selective sensing under operational conditions. In particular, while several analytes, including water, exhibit highly negative ΔG values at room temperature, potentially leading to irreversible surface saturation, increasing the temperature to 150 °C reduces the free energy gain associated with their adsorption. This thermal modulation is especially critical for water, whose strong interaction with oxide-based surfaces can passivate the adsorption sites and suppress the sensitivity.

A critical analysis of the differential Gibbs free energy (ΔG) values at 150 °C is presented in Table 2, enabling a more accurate assessment of the selective adsorption properties of the Ga_2O_3-based substrates. The adsorption of ammonia (NH_3) remains markedly exergonic across all substrates, with ΔG values ranging from −145.6 kJ mol^{-1} on Ga_2O_3 to −68.7 kJ mol^{-1} on $Ga_2O_{2\cdot98}$, indicating that thermodynamically stable adsorption persists even at elevated temperatures. Among the nontetragonal substrates, Ga_2O_3 and $Ga_{98}S_{n\cdot n2}$ exhibit the most negative ΔG values (−145.6 and −86.3 kJ mol^{-1}, respectively), which confirms their strong affinity for NH_3 and suggests that they are the most suitable platforms for ammonia sensing.

In contrast, for NO_2, the ΔG values at 150 °C exhibited a qualitatively different trend, although t-$Ga_2O_{2\cdot98}S_{n\cdot n2}$ and t-Ga_2O_3 show significantly negative ΔG (−120.5 and −93.2 kJ mol^{-1}), the nontetragonalized $Ga_2O_{2\cdot98}$ also exhibits a surprisingly strong interaction, with ΔG = −115.7 kJ mol^{-1}. This suggests a distinct adsorption mechanism, possibly involving oxygen vacancies acting as preferential adsorption sites, a hypothesis supported by the charge density redistribution observed in Figure 8c.

The case of CO is even more illustrative in terms of the effect of the tetragonal distortion on the selectivity. ΔG values for CO adsorption on tetragonalized Ga_2O_3 and $Ga_2O_{2\cdot98}S_{n\cdot n2}$ (−133.9 and −138.8 kJ mol^{-1}, respectively) are clearly more favorable than their nontetragonalized counterparts. This implies that tetragonalization modulates the local electronic structure in a manner that enhances the CO affinity, possibly through enhanced orbital overlap or modified dipole interactions at adsorption sites. Thus, the structural transformation induced by tetragonalization appears to switch the adsorption preference from NH_3 (in the nontetragonalized case) to CO (in the tetragonalized case).

The selectivity of the experimental GaS sensor, which was operated at 150 °C and showed a clear response only to NH_3 (with a measured sensitivity of 18%, Figure 9b), can be rationalized in terms of its surface composition and structure. The native oxide layer formed upon ambient exposure, as shown in the TEM and XPS data, is consistent with the formation of a nontetragonalized Ga_2O_3-like phase, possibly due to sulfur substitution (that is, $Ga_2O_{2\cdot98}S_{n\cdot n2}$). According to the theoretical model, this exact configuration displays strong and selective NH_3 adsorption at 150 °C, while ΔG values for other species such as NO_2 (−29.9 kJ mol^{-1}), CO (−69.4 kJ mol^{-1}), and H_2 (−3.9 kJ mol^{-1}) are significantly less favorable.

Therefore, the experimental selectivity of the GaS-based sensor toward NH_3 can be confidently attributed to the formation of a surface oxide skin that mimics either Ga_2O_3 or $Ga_2O_{2\cdot98}S_{n\cdot n2}$ in their nontetragonalized forms, which are thermodynamically predisposed to bind to NH_3 rather than competing analytes. In

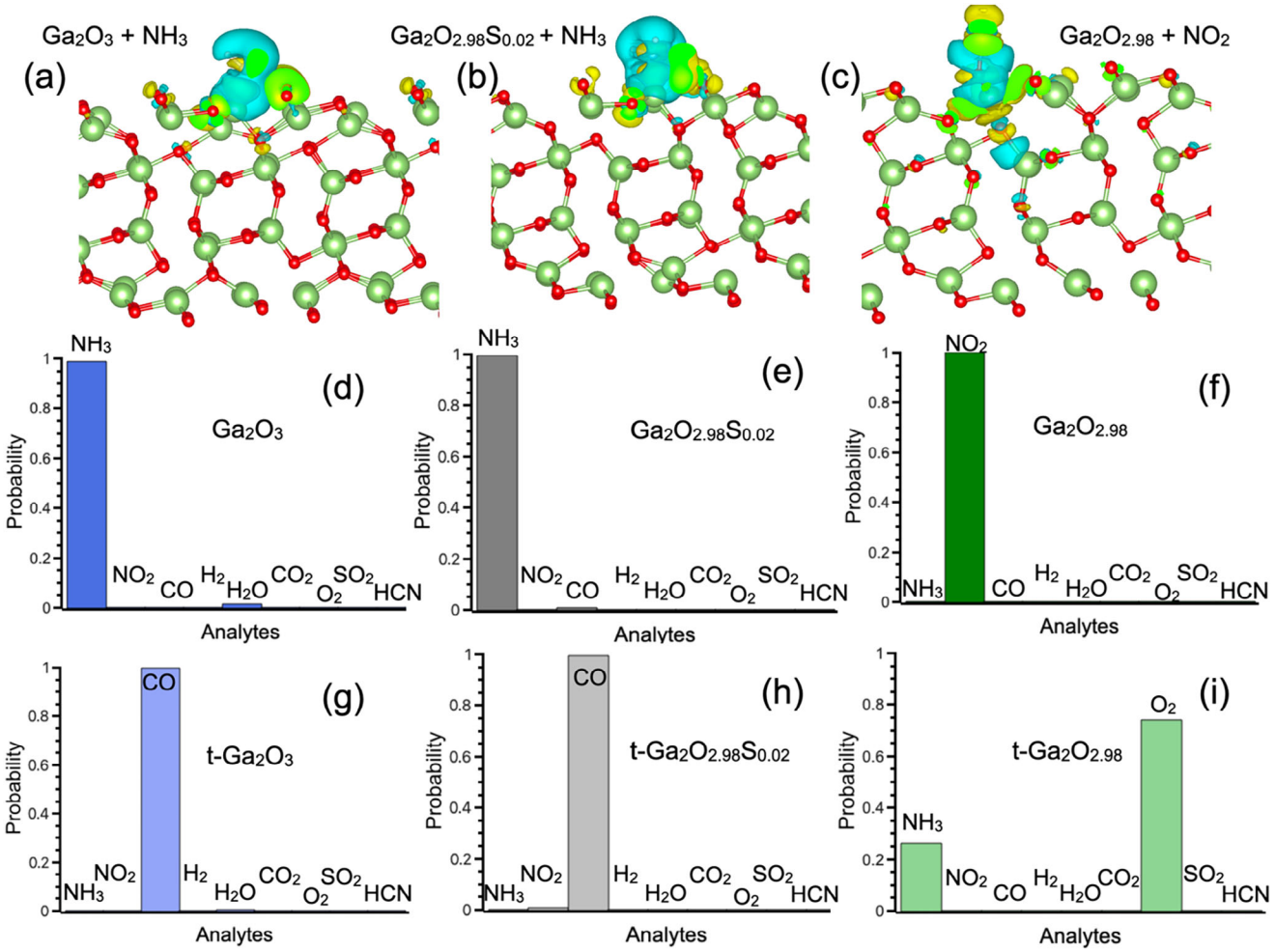

Figure 8. Charge redistribution after adsorption of ammonia on nontetragonalized surfaces of a) Ga_2O_3, b) $Ga_2O_{2.98}S_{0.02}$ slabs, and c) NO_2 on the surface of $Ga_2O_{2.98}$ slab. The yellow and cyan clouds correspond to increased and decreased charge densities, respectively. Panels d-i) show the probabilities of analyte adsorption on the surfaces of d–f) nontetragonalized and g–i) tetragonalized Ga_2O_3, $Ga_2O_{2.98}S_{0.02}$, and $Ga_2O_{2.98}$ slabs, respectively, at 150 °C.

this context, the observed charge redistribution extending into the subsurface regions (Figure 8a,b) further supports the idea that NH_3 adsorption induces a measurable electronic perturbation, thus triggering a resistive response in the sensor.

The theoretical selectivity trends were further supported by the Boltzmann-weighted adsorption probabilities computed at 150 °C, as shown in **Figure 8** (panels d–i). These probabilities, derived from the calculated Gibbs free energies, reflect the thermodynamic probability of an analyte populating a specific adsorption site at the operating temperature of the sensor. For nontetragonalized Ga_2O_3 and $Ga_2O_{2\cdot98}S_{n\cdot n2}$ (Figure 8d,e), NH_3 emerges as the dominant adsorbed species, with negligible occupancy by competing molecules such as CO, NO_2, or H_2. This is consistent with the strongly negative ΔG values discussed previously and provides a thermodynamically grounded rationale for the observed selectivity in the experimental GaS sensor.

The situation changes dramatically in the tetragonalized phases (Figure 8g–i), where the adsorption probability of CO increases significantly, often exceeding that of NH_3. This transition in selectivity can be traced directly to the relative stabilization of CO adsorption upon tetragonalization, as evidenced by the higher ΔG values for CO on t-Ga_2O_3 and t-$Ga_2O_{2\cdot98}S_{n\cdot n2}$. In essence, tetragonalization acts as a structural switch, shifting the selectivity landscape from a preference for NH_3 to CO.

Oxygen-deficient $Ga_2O_{2\cdot98}$ surface occupies an intermediate regime. While it still exhibits selective NH_3 adsorption at room temperature, the adsorption probabilities at 150 °C show a substantial enhancement for NO_2, reflecting the pronounced thermodynamic driving force (ΔG = −115.7 kJ mol^{-1}). This behavior supports the assignment of oxygen vacancies as specific chemisorption sites for oxidizing analytes, which is further corroborated by the localized charge accumulation shown in Figure 8c.

Experimentally, the response of the GaS sensors to ammonia was studied at different operating temperatures ranging from 25 to 350 °C. The optimal operating temperature, within the range tested for detecting ammonia vapors (i.e., the temperature that led to a higher sensor response), was 150 °C (Table S2, Supporting Information). **Figure 9a** shows the dynamic response of the GaS sensor to two consecutive exposure and recovery cycles at

Table 2. Differential enthalpy (ΔH) and Gibbs free energy (ΔG) for physisorption at room temperature (*RT*) and 150 °C for the selected analytes on Ga_2O_3, $Ga_2O_{2.98}S_{0.02}$, and $Ga_2O_{2.98}$ surfaces. Tetragonalized substrates are denoted with "t-.".

Analyte	Substrate	ΔH	ΔG	
			RT	150 °C
NH_3	Ga_2O_3	−176.3	−154.7	−145.6
	t-Ga_2O_3	−137.4	−115.8	−106.7
	$Ga_2O_{2.98}S_{0.02}$	−117.0	−95.4	−86.3
	t-$Ga_2O_{2.98}S_{0.02}$	−137.6	−116.0	−106.9
	$Ga_2O_{2.98}$	−99.4	−77.8	−68.7
	t-$Ga_2O_{2.98}$	−137.4	−115.8	−106.7
NO_2	Ga_2O_3	−44.6	−11.5	+2.4
	t-Ga_2O_3	−140.2	−140.2	−93.2
	$Ga_2O_{2.98}S_{0.02}$	−76.9	−43.8	−29.9
	t-$Ga_2O_{2.98}S_{0.02}$	−167.5	−134.4	−120.5
	$Ga_2O_{2.98}$	−68.7	−35.6	−115.7
	t-$Ga_2O_{2.98}$	−62.0	−28.9	−15.0
CO	Ga_2O_3	−122.4	−103.0	−94.9
	t-Ga_2O_3	−161.4	−142.0	−133.9
	$Ga_2O_{2.98}S_{0.02}$	−97.0	−77.6	−69.4
	t-$Ga_2O_{2.98}S_{0.02}$	−166.3	−146.9	−138.8
	$Ga_2O_{2.98}$	−42.6	−23.2	−15.1
	t-$Ga_2O_{2.98}$	−35.3	−15.9	−7.8
H_2	Ga_2O_3	+6.4	+14.6	+18.0
	t-Ga_2O_3	−3.4	+4.8	+8.2
	$Ga_2O_{2.98}S_{0.02}$	−7.7	+0.5	+3.9
	t-$Ga_2O_{2.98}S_{0.02}$	−7.8	+0.4	+4.0
	$Ga_2O_{2.98}$	−80.7	−72.5	−69.1
	t-$Ga_2O_{2.98}$	−10.8	−2.6	+0.1
H_2O	Ga_2O_3	−177.0	−144.4	−130.7
	t-Ga_2O_3	−160.7	−128.1	−114.4
	$Ga_2O_{2.98}S_{0.02}$	−88.4	−54.9	−42.1
	t-$Ga_2O_{2.98}S_{0.02}$	−110.7	−78.1	−64.4
	$Ga_2O_{2.98}$	−97.0	−56.9	−50.7
	t-$Ga_2O_{2.98}$	−92.6	−60.0	−46.3
CO_2	Ga_2O_3	+26.5	+43.8	+51.1
	t-Ga_2O_3	−17.0	+0.3	+7.55
	$Ga_2O_{2.98}S_{0.02}$	−6.3	+11.0	+18.3
	t-$Ga_2O_{2.98}S_{0.02}$	−33.2	−15.9	−8.6
	$Ga_2O_{2.98}$	−20.9	−3.6	+3.7
	t-$Ga_2O_{2.98}$	−25.3	−8.0	−‘0.7
O_2	Ga_2O_3	−48.4	−16.0	−2.4
	t-Ga_2O_3	−47.3	−14.9	−1.3
	$Ga_2O_{2.98}S_{0.02}$	−47.7	−15.3	−1.7
	t-$Ga_2O_{2.98}S_{0.02}$	−83.6	−51.2	−37.6
	$Ga_2O_{2.98}$	−63.9	−31.5	−17.9
	t-$Ga_2O_{2.98}$	−156.4	−124.0	−110.4
SO_2	Ga_2O_3	−17.0	+19.2	+34.4
	t-Ga_2O_3	−1.9	+34.3	+49.5
	$Ga_2O_{2.98}S_{0.02}$	−47.6	−11.4	+3.8
	t-$Ga_2O_{2.98}S_{0.02}$	−48.8	−12.6	+2.6
	$Ga_2O_{2.98}$	−46.9	−10.7	+4.5
	t-$Ga_2O_{2.98}$	−5.0	+31.2	+46.4
HCN	Ga_2O_3	−4.9	+20.3	+30.9
	t-Ga_2O_3	−78.9	−53.7	−43.1
	$Ga_2O_{2.98}S_{0.02}$	−40.5	−15.3	−4.7
	t-$Ga_2O_{2.98}S_{0.02}$	−83.2	−58.0	−47.4
	$Ga_2O_{2.98}$	−56.4	−31.2	−20.6
	t-$Ga_2O_{2.98}$	−65.0	−39.8	−29.2

30 ppm of ammonia (see Figure 9b for the determination of response and recovery times). At the optimal operating temperature for ammonia detection, the sensor was exposed to other gaseous species, such as nitrogen dioxide, hydrogen, carbon dioxide, and ethanol.

The selectivity profile shown in Figure 9c shows a distinct preference for NH_3 over other gases such as NO_2, H_2, CO_2, and ethanol. The sensor response at 150 °C, characterized by a relative resistance change of 18%, aligns well with the adsorption thermodynamics of NH_3 on Ga_2O_3-type surfaces. It is plausible that the active surface resembled nontetragonalized $Ga_2O_{2\cdot 98}S_{n\cdot n2}$. This would place the sensor operation in a regime of maximal NH_3 selectivity, as predicted by both the ΔG values and the Boltzmann-weighted adsorption probabilities.

Moreover, the extended charge redistribution induced by NH_3 adsorption (Figure 8a,b) implies a depth-dependent electronic perturbation, which likely manifests as a modulation of the surface potential or carrier density. This, in turn, produced a measurable resistive response, as captured in the dynamic measurements shown in Figure 9a. Despite its strong adsorption on $Ga_2O_{2.98}$, there is no comparable response to NO_2, confirming that the surface structure plays a decisive role: either oxygen-deficient domains are not dominant on the oxidized GaS surface, or NO_2 adsorption does not induce sufficient carrier modulation owing to localization effects or limited interaction with the conduction channel.

To rationalize the experimental observation of the decreased sensor response to ammonia at operating temperatures exceeding 150 °C (Table S2, Supporting Information), we performed theoretical calculations of the saturation of active surface sites available for the competitive adsorption of NH_3 and O_2 molecules on the investigated Ga_2O_3-based substrates. Specifically, we employed Langmuir adsorption isotherms to evaluate the influence of temperature on the occupancy of surface sites by NH_3 molecules from a mixture containing 30 ppm ammonia, simulating the experimental sensing conditions. The results shown in Figure S8 (Supporting Information) reveal markedly different temperature-dependent behaviors across the studied surfaces. In particular, the saturation curves clearly show that, the two substrates identified experimentally and theoretically as highly selective toward ammonia (namely, pure Ga_2O_3 and the sulfur-substituted variant $Ga_2O_{2\cdot 98}S_{n\cdot n2}$), the temperature threshold at which active site saturation begins to decline notably differs. While pure Ga_2O_3 maintains a high NH_3 occupancy at temperatures as high as ≈500 °C, $Ga_2O_{2\cdot 98}S_{n\cdot n2}$ shows a significant drop in the NH_3 site coverage starting at ≈200 °C. Notably, this theoretically predicted temperature closely matches the experimental observation, where the optimal sensing temperature was identified as ≈150 °C, with a measurable decline in sensitivity at higher temperatures than this value.

These theoretical insights strongly support the hypothesis that the experimentally observed oxide layer formed on GaS surfaces exposed to air primarily consists of Ga oxide incorporating substitutional sulfur impurities inherited from the parent GaS material during oxidation. Indeed, there is a close correspondence between the calculated temperature range for optimal NH_3 adsorption on $Ga_2O_{2\cdot 98}S_{n\cdot n2}$ surfaces and the experimental sensing window observed in GaS-based sensors, providing compelling evidence that the active surface sites involved in ammonia sensing

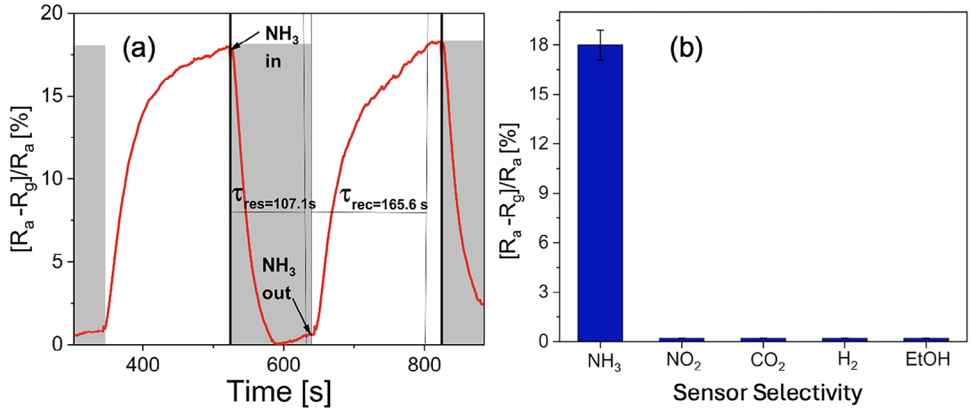

Figure 9. a) Typical response of the GaS sensor to consecutive cycles of exposure to 30 ppm NH_3 and recovery in dry air. The sensor was operated at 150 °C. The sensor response (%) was defined as $100 \times (R_a - R_g)/R_a$, where R_a is the baseline resistance in dry air and R_g is the resistance upon ammonia exposure. Response (τ_{res}) and recovery (τ_{rec}) times were determined as the time intervals needed to reach 90% of the total resistance change upon exposure and during recovery, respectively, resulting in values of $\tau_{res} = 107.1$ s and $\tau_{rec} = 165.6$ s. b) Selectivity analysis of the sensors. Comparison of responses to ammonia (30 ppm), nitrogen dioxide (10 ppm), hydrogen (1000 ppm), carbon dioxide (500 ppm), and ethanol (25 ppm). The operating temperature of the sensor was 150 °C.

are related to sulfur-doped gallium oxide phases rather than pure gallium oxide.

To evaluate the long-term reliability of GaS-based ammonia sensors, we conducted stability tests by repeating the NH_3 sensing experiments after a three-month storage period under ambient laboratory conditions. During this time, the devices were kept inside the measurement chamber but were not encapsulated; thus, they remained continuously exposed to air with fluctuating relative humidity (35–50%) and temperature (21–23 °C). This approach was designed to simulate realistic operating conditions in the absence of protective packaging. After this period, the sensors remained fully functional, and their qualitative response to ammonia was still clearly observable. Nevertheless, a quantitative degradation of the signal intensity was detected, with an average decrease of ≈55 ± 5% compared to the initial measurements. This result highlights that, although the sensing mechanism remains active, prolonged exposure to ambient conditions leads to a progressive decline in sensitivity, which should be addressed in future efforts toward device stabilization and encapsulation strategies.

2.5. Thermal Stability

The thermal stability of the GaS crystals was thoroughly investigated using a series of complementary characterization techniques, including energy-dispersive X-ray spectroscopy (EDX), XRD, thermogravimetric analysis (TGA), and differential scanning calorimetry (DSC), as detailed in the Supporting Information (Figures S5–S7). Specifically, EDX analysis (Figure S5, Supporting Information) revealed no qualitative changes in the elemental composition after annealing GaS in a nitrogen atmosphere for 2 min at temperatures ranging from 200 to 800 °C, thus confirming the compositional stability and negligible chemical modification under thermal stress conditions. Additionally, the XRD patterns (Figure S6, Supporting Information) collected under identical annealing conditions further corroborated the remarkable structural stability, exhibiting no detectable phase transitions or crystallographic modifications even at the highest temperature tested (800 °C). Finally, simultaneous thermal analysis (TGA/DSC, Figure S7, Supporting Information) showed minimal weight loss and the absence of significant calorimetric transitions, confirming that GaS maintains high thermal and chemical integrity within the investigated temperature range. These combined results unambiguously demonstrate the exceptional thermal stability of GaS, underpinning its suitability for high-temperature sensing and catalytic applications.

3. Conclusion

In this study, we demonstrated the exceptional catalytic and gas-sensing capabilities of self-assembled heterostructures formed by GaS with its native oxide by combining advanced surface science experiments with theoretical modeling. Our findings clearly establish that the controlled formation of surface sulfur vacancies and the development of nanoscale native oxide layers significantly enhance the catalytic performance of GaS-based materials for water splitting and their selective and ultrasensitive ammonia-sensing capabilities.

The combined experimental and theoretical analyses revealed the critical role of sulfur vacancies in tuning the reactivity of GaS surfaces. Specifically, our calculations indicate a high energy barrier (205.5 kJ mol^{-1}) for sulfur layer displacement on pristine GaS surfaces, suggesting excellent stability against spontaneous oxidation during initial exposure to ambient conditions. This intrinsic stability is essential for the long-term durability of the catalyst. However, once sulfur vacancies are formed, the catalytic properties of GaS change dramatically because of prolonged exposure to oxidizing environments. For instance, although the energy cost for water decomposition is prohibitively high on defect-free GaS surfaces (419.3 kJ mol^{-1}), the introduction of surface sulfur vacancies markedly reduces this barrier to −147.6 kJ mol^{-1} on $GaS_{n\cdot 96}$, thereby enabling a highly efficient HER under alkaline conditions.

The catalytic efficiency of defective GaS ($GaS_{n\cdot 96}$) in alkaline HER was further validated by evaluating the differential free energies involved in each reaction step, which showed notably favorable energetics (−1.56 eV for hydroxyl adsorption and +1.28 eV for subsequent desorption). Conversely, we demonstrated that GaS-based catalysts are unsuitable for the HER in acidic media because of their significantly higher reaction energies (>0.7 eV), thus clearly defining their applicability range and guiding the selection of appropriate operating conditions.

In contrast, GaS-based heterostructures show considerable promise for the OER. Our results indicate that all reaction steps for the OER on $GaS_{n\cdot 96}$ surfaces were exothermic, emphasizing the favorable impact of sulfur vacancies. Similarly, native oxide-covered structures (Ga_2S_2O) show a mostly exothermic reaction path, with only the final reaction step having a moderate energy cost (0.96 eV). These observations highlight how defect engineering and controlled oxidation critically modulate surface reactivity and catalytic performance.

The impact of native oxide formation on the sensing capabilities of GaS-based heterostructures was equally significant. Experimentally, we observed remarkable sensitivity (response of 18%) and unprecedented selectivity for ammonia detection at moderate operating temperatures (150 °C), which is consistent with theoretical predictions. This superior performance is attributed to the strong ammonia binding at the Ga_2O_{3-x}/GaS interface, coupled with substantial charge transfer interactions that effectively translate molecular adsorption into measurable electrical signals. This result indicates that GaS heterostructures exhibit both exceptional sensitivity and strong selectivity, which are crucial for effective gas-sensing applications in environmental monitoring.

Our findings suggest that GaS-based heterostructures are versatile multifunctional platforms with substantial potential for application in next-generation sustainable technologies. Their intrinsic stability under realistic operating conditions, coupled with highly tunable catalytic and sensing functionalities, makes these heterostructures promising candidates for renewable energy solutions, such as photoelectrochemical water splitting, and highly sensitive environmental sensors. Future research should focus on optimizing defect densities through advanced synthesis techniques, exploring scale-up routes for device integration, and conducting long-term stability assessments in operational environments. Furthermore, in response to the growing demand for practical deployment of GaS-based materials in energy and sensing technologies, we emphasize the feasibility of scalable production is supported by the compatibility of GaS with liquid-phase exfoliation protocols. From an economic perspective, the relative abundance of gallium and sulfur, coupled with the elimination of noble metal catalysts, strongly reduces material-related costs. Moreover, the robustness of the self-assembled Ga_2O_3/GaS heterostructure under operational conditions ensures minimal performance loss over time. These attributes define a promising roadmap toward the integration of GaS-based devices in real-world applications.

4. Experimental Section

Single-Crystal Growth: The Bridgman-Stockbarger method was used to grow single-crystal GaS ingots. Initially, a cleaned quartz glass ampule with a length of 250 mm and an inner diameter of 10 mm was filled with stoichiometric amounts of high-purity Ga and S, corresponding to 20 g of the final compound. A diffusion pump was used to evacuate the ampoule to a pressure of approximately 10^{-6} Torr, and an oxygen-acetylene torch was used to close the ampoule. The ampule was placed in a handmade furnace in two different temperature zones, and the growth process was performed according to the temperature program.

XRD: To determine the crystal structure of bulk GaS, XRD measurements were conducted using a Bruker D2 Phaser diffractometer, which utilizes Cu-Kα radiation (1.5406 Å) in scanning mode from 10°to 90° 2θ with a step size of 0.02°.

TEM: FEI TALOS F200S (200 kV) HR-TEM was used for the morphological analysis of GaS nanosheets. Samples for TEM experiments were prepared by liquid-phase exfoliation using a dispersion of 10 mg of powdered GaS bulk crystal in 25 mL of N-methyl-2-pyrroliolidine (NMP) solvent. The resulting mixture was sonicated in a Bandelin ultrasonic bath at room temperature (vibration frequency of 35 kHz) for 7 h. Finally, 10 µL of GaS-based ink was dropped onto a copper grid surface under ambient conditions.

ARPES: High-resolution ARPES studies were conducted at the URANOS beamline of the Solaris Synchrotron in Krakow, Poland.[83] The beamline was equipped with a Scienta-Omicron DA30-L electron analyzer. Single-crystal samples were mechanically exfoliated using adhesive tape under ultrahigh vacuum (10^{-8} mbar) at ambient temperature. The pressure during the ARPES measurement was maintained below 5×10^{-11} mbar, and the temperature during the experiment was kept at 79 K.

LEED: Micro Low-Energy Electron Diffraction (µ-LEED) measurements were conducted using a spectroscopic photoemission and low-energy electron microscope (SPELEEM III, Elmitec GmbH) at the "Nanospectroscopy" beamline of the Elettra synchrotron in Trieste, Italy. The microscope performed µ-LEED by placing apertures of 0.5, 1, or 5 µm in diameter in the image plane. The electron energy was controlled by applying a voltage bias to the sample, which is commonly referred to as the starting voltage. The SPELEEM microscope was equipped with a hemispherical energy analyzer (Elmitec R200), which provided the best energy resolution of 100 meV in diffraction mode. The base pressure of the experimental chamber was maintained below 2×10^{-10} mbar.

Theory: The atomic structure, energetics of various configurations, and interactions were studied using DFT with the QUANTUM-ESPRESSO code[84] with GGA–PBE,[85] considering the van der Waals-like force correction.[86] Ultrasoft pseudopotentials[87] were used for all simulations, with energy cutoffs of 35 and 400 Ry for the plane-wave expansion of the wave functions and charge density, respectively. The differential physisorption enthalpies were calculated using the following standard formula:

$$\Delta H_{phys} = \left[E_{subst+mol} - (E_{subst} + E_{mol})\right] \quad (2)$$

where E_{subst} is the total energy of the substrate, and E_{mol} is the energy of the single molecules of the selected species in an empty box. Only the gaseous phase was considered for the water adsorption. The decomposition energy is defined as the difference between the total energy of the system with an adsorbed molecule and that of the same system after decomposition on the surface. For physisorption, the differential Gibbs free energy at a given temperature was calculated using the following formula:

$$\Delta G = \Delta H - T\Delta S \quad (3)$$

where T is the temperature and ΔS is the change in entropy of the adsorbed molecule. The change in entropy ΔS was estimated by considering the gas-to-liquid transition using the following equation:

$$\Delta S = \Delta H_{vaporisation}/T \quad (4)$$

where, $\Delta H_{vaporization}$ is the measured enthalpy of vaporization.

To test the technical parameters, we optimized the atomic structure of bulk GaS. Good convergence between the theoretical and experimen-

tal lattice parameters was achieved only for large-energy cutoff values. A 3 × 3 supercell was used to simulate the surfaces of the bulk crystal and monolayer. To simulate the bulk, we used a GaS bilayer with fixed lattice parameters obtained from bulk calculations. Only the atomic positions were optimized in this study. This type of calculation imitates the effect of the rigid subsurface bulk part of the crystal on the structure and properties of the surface layers. The lattice parameters and atomic positions were optimized to simulate flexible monolayers. The isosurface level in Figure 7a–c is 5×10^{-4} e^{-}Å^{-3}.

Synchrotron-Based XPS: Synchrotron-based XPS measurements were performed at the Elettra synchrotron in Trieste, Italy, on the BACH beamline. XPS measurements were performed using a Scienta R3000 hemispherical electron analyzer at room temperature. The spectra were recorded in normal incidence geometry and calibrated using Au-4f from a gold foil in electrical contact with the samples. Pure O_2 gas was dosed into a high-pressure chamber with a base pressure of $<5 \times 10^{-8}$ mbar and connected to the measurement chamber at room temperature. The Shirley background was subtracted from the raw data.

Gas Sensor Preparation: GaS nanosheets were produced via liquid-phase exfoliation (LPE) by dispersing bulk GaS crystals in N-methyl-2-pyrrolidone (NMP), followed by ultrasonication and centrifugation to isolate and purify the exfoliated nanosheets. The obtained nanosheets had an average lateral size of ≈2 µm, as evident from the X-ray photoemission electron microscopy (XPEEM) results shown in Figure S4 in the S5Supporting Information. The GaS suspension was deposited onto SiO_2/Si substrates comprising interdigitated Au electrodes with a 5 µm electrode gap. These substrates were attached to a commercially available alumina plate featuring a platinum resistive heating meander on its back to enable the setting of the operating temperature of the sensors. Each substrate was airbrushed with 90 µL of the solution and kept on a hotplate at 90 °C.

Gas Sensing Measurements: A 35 mL Teflon chamber with a home-made gas mixture and delivery system was used to test the sensor. The chamber can accommodate up to four sensors. The resistance of the sensors was monitored using a Keysight BenchVue data-collection system. Bronkhorst mass flow controllers were used to generate and deliver reproducible concentrations of different gaseous species to the sensor chamber for testing. Calibrated cylinders of NH_3, NO_2, CO_2, H_2, and ethanol diluted in zero-grade dry air were used. A constant flow rate of 100 mL min^{-1} was maintained throughout the measurements. The sensor response (%) was defined as $100 \times (R_a - R_g)/R_a$, where R_a is the baseline resistance measured in dry air, and R_g is the sensor resistance during exposure to the target gas. The response and recovery times were calculated as the times required to reach 90% of the full response and recovery, respectively.

Supporting Information

Supporting Information is available from the Wiley Online Library or from the author.

Acknowledgements

D.W.B. and T.D. contributed equally to this work. This work was funded by the European Commission- Next Generation EU, Mission 4Component C2, Investment 1.1, under the Ministry of University and Research (MUR) of Italy PRIN 2022 (CUP: E53D23001750006, Grant No. 2022LFWJBR, acronym PLANET) and PRIN PNRR (CUP: E53D23018280001, Grant No. P20223LXTA, acronym ENTANGLE) projects. T.D. and A.P. acknowledges the financial support of the European Union's Horizon Europe Research and Innovation Programme under the project EXBRINER "Next-generation membrane technologies for sustainable exploitation of seawater brine resources: transition toward a circular blue industry" (HORIZON-MSCA-DN-2021, Grant Agreement No. 101072449). The authors acknowledge the SOLARIS Synchrotron and Elettra Synchrotron Trieste for providing access to experimental facilities. This publication is part of the project PNRR-NGEU which has received funding from the MUR-DM118/2023 and MUR-DM630/2024. The authors are grateful to Süleyman Tekmen (University of Bayburt, Central Research Laboratory, Bayburt, Turkey) for his support with the TEM experiments. J.S. is supported by Grant No. 2022 FI SDUR 00307 of the Department of Research and Universities of the Government of Catalonia (AGAUR) and the European Social Plus Fund. E.L. is supported by the Catalan Institution for Research and Advanced Studies (ICREA) via the 2023 Edition of the ICREA Academia Award.

Open access publishing facilitated by Universita degli Studi dell'Aquila, as part of the Wiley - CRUI-CARE agreement.

Conflict of Interest

The authors declare no conflict of interest.

Data Availability Statement

The data that support the findings of this study are available from the corresponding author upon reasonable request.

Keywords

2D materials, ammonia sensing, DFT calculations, hydrogen evolution reaction, X-ray photoelectron spectroscopy (XPS)

Received: March 23, 2025
Revised: May 18, 2025
Published online: June 9, 2025

[1] W. Su, A. Kuklin, L. Jin, H. Ågren, Y. Zhang, *Adv. Funct. Mater.* **2024**, *34*, 2405752.
[2] Z. Li, K. Li, Y. Li, Y. Yu, J. Lv, X. Liu, K. Guan, W. Lei, S. Zhang, H. Zhang, *Adv. Funct. Mater.* **2024**, *34*, 2310371.
[3] C. Liu, P. Zhao, K. Lu, S. Han, C. Zhang, X. Xia, W. Lei, Q. Guo, Q. Hao, *Adv. Funct. Mater.* **2024**, *34*, 2401392.
[4] Y. Guan, Y. Ding, Y. Fang, F. Zhou, J. Wang, X. Li, S. Zhao, B. Gao, C. Xu, L. Zhen, F. Huang, L. Yang, Y. Li, *Adv. Funct. Mater.* **2024**, *34*, 2400965.
[5] F. Pei, J. Yu, J. Zhou, S. Wang, D. Liu, Y. Yuan, L. Xi, F. Jin, X. Kan, C. Wang, L. Wang, W. Yan, Y. Wu, S. Wang, K. Chen, T. Ma, X. Liu, M. Yang, Q. Li, *Adv. Funct. Mater.* **2024**, *34*, 2309335.
[6] Y. Liu, Q. Gong, Y. Yin, M. Yi, Y. Liu, *Adv. Funct. Mater.* **2024**, *34*, 2310372.
[7] J. Duan, D. S. Ma, R. W. Zhang, W. Jiang, Z. Zhang, C. Cui, Z. M. Yu, Y. Yao, *Adv. Funct. Mater.* **2024**, *34*, 2313067.
[8] R. Dong, X. Gong, J. Yang, Y. Sun, J. Wang, L. Ma, *Adv. Funct. Mater.* **2024**, *34*, 2310346.
[9] G. A. Somorjai, Y. Li, *Proc. Natl. Acad. Sci., USA* **2011**, *108*, 917.
[10] C. Anichini, W. Czepa, D. Pakulski, A. Aliprandi, A. Ciesielski, P. Samorì, *Chem. Soc. Rev.* **2018**, *47*, 4860.
[11] Q. Fu, X. Bao, *Chem. Soc. Rev.* **2017**, *46*, 1842.
[12] Y. Sun, S. Gao, F. Lei, Y. Xie, *Chem. Soc. Rev.* **2015**, *44*, 623.
[13] X. Zhang, A. Chen, L. Chen, Z. Zhou, *Adv. Energy Mater.* **2022**, *12*, 2003841.
[14] J. Shu, D. Tang, *Anal. Chem.* **2019**, *92*, 363.
[15] Y. Shi, L. Ni, Z. Wang, M. Chen, L. Feng, *Coord. Chem. Rev.* **2024**, *505*, 215691.
[16] K. F. Mak, C. Lee, J. Hone, J. Shan, T. F. Heinz, *Phys. Rev. Lett.* **2010**, *105*, 136805.
[17] A. Splendiani, L. Sun, Y. Zhang, T. Li, J. Kim, C.-Y. Chim, G. Galli, F. Wang, *Nano Lett.* **2010**, *10*, 1271.

[18] K. Xu, L. Yin, Y. Huang, T. A. Shifa, J. Chu, F. Wang, R. Cheng, Z. Wang, J. He, *Nanoscale* **2016**, *8*, 16802.
[19] S. Lei, F. Wen, L. Ge, S. Najmaei, A. George, Y. Gong, W. Gao, Z. Jin, B. Li, J. Lou, *Nano Lett.* **2015**, *15*, 3048.
[20] R. B. Jacobs-Gedrim, M. Shanmugam, N. Jain, C. A. Durcan, M. T. Murphy, T. M. Murray, R. J. Matyi, R. L. Moore, B. Yu, *ACS Nano* **2014**, *8*, 514.
[21] Y. Wang, K. Szökölová, M. Z. M. Nasir, Z. Sofer, M. Pumera, *ChemCatChem* **2019**, *11*, 2634.
[22] X. Li, M.-W. Lin, A. A. Puretzky, J. C. Idrobo, C. Ma, M. Chi, M. Yoon, C. M. Rouleau, I. I. Kravchenko, D. B. Geohegan, *Sci. Rep.* **2014**, *4*, 5497.
[23] X. Li, L. Basile, B. Huang, C. Ma, J. Lee, I. V. Vlassiouk, A. A. Puretzky, M.-W. Lin, M. Yoon, M. Chi, *ACS Nano* **2015**, *9*, 8078.
[24] C. S. Jung, F. Shojaei, K. Park, J. Y. Oh, H. S. Im, D. M. Jang, J. Park, H. S. Kang, *ACS Nano* **2015**, *9*, 9585.
[25] Y. Ma, Y. Dai, M. Guo, L. Yu, B. Huang, *Phys. Chem. Chem. Phys.* **2013**, *15*, 7098.
[26] C. Jastrzebski, K. Olkowska, D. J. Jastrzebski, M. Wierzbicki, W. Gebicki, S. Podsiadlo, *J. Phys.: Cond. Matt.* **2019**, *31*, 075303.
[27] T. M. Brenner, D. A. Egger, L. Kronik, G. Hodes, D. Cahen, *Nat. Rev. Mater.* **2016**, *1*, 15007.
[28] S. M. Sze, Y. Li, K. K. Ng, *Physics of semiconductor devices*, John Wiley & Sons, Hoboken, NJ, **2021**.
[29] W. Huang, L. Gan, H. Li, Y. Ma, T. Zhai, *CrystEngComm* **2016**, *18*, 3968.
[30] P. Hu, L. Wang, M. Yoon, J. Zhang, W. Feng, X. Wang, Z. Wen, J. C. Idrobo, Y. Miyamoto, D. B. Geohegan, K. Xiao, *Nano Lett.* **2013**, *13*, 1649.
[31] S. Yang, Y. Li, X. Wang, N. Huo, J.-B. Xia, S.-S. Li, J. Li, *Nanoscale* **2014**, *6*, 2582.
[32] D. J. Late, B. Liu, J. Luo, A. Yan, H. S. S. R. Matte, M. Grayson, C. N. R. Rao, V. P. Dravid, *Adv. Mater.* **2012**, *24*, 3549.
[33] P. Marvan, V. Mazánek, Z. Sofer, *Nanoscale* **2019**, *11*, 4310.
[34] H. L. Zhuang, R. G. Hennig, *Chem. Mater.* **2013**, *25*, 3232.
[35] A. Harvey, C. Backes, Z. Gholamvand, D. Hanlon, D. McAteer, H. C. Nerl, E. McGuire, A. Seral-Ascaso, Q. M. Ramasse, N. McEvoy, S. Winters, N. C. Berner, D. McCloskey, J. F. Donegan, G. S. Duesberg, V. Nicolosi, J. N. Coleman, *Chem. Mater.* **2015**, *27*, 3483.
[36] J. Luxa, Y. Wang, Z. Sofer, M. Pumera, *Chem. - Eur. J.* **2016**, *22*, 18810.
[37] J. Casanova-Chafer, R. Garcia-Aboal, P. Atienzar, E. Llobet, *ACS Sens.* **2022**, *7*, 3753.
[38] J. Kangsabanik, M. K. Svendsen, A. Taghizadeh, A. Crovetto, K. S. Thygesen, *J. Am. Chem. Soc.* **2022**, *144*, 19872.
[39] C. Ho, S. Lin, *J. Appl. Phys.* **2006**, 100.
[40] S. Tang, W. Qiu, S. Xiao, Y. Tong, S. Yang, *Energy Environ. Sci.* **2020**, *13*, 660.
[41] V. O. Jimenez, Y. T. H. Pham, D. Zhou, M. Liu, F. A. Nugera, V. Kalappattil, T. Eggers, K. Hoang, D. L. Duong, M. Terrones, H. Rodriguez Gutiérrez, M.-H. Phan, *Adv. Sci.* **2024**, *11*, 2304792.
[42] Y. Guo, S. Zhou, Y. Bai, J. Zhao, *J. Chem. Phys.* **2017**, *147*, 104709.
[43] Q. Li, Q. Zhou, L. Shi, Q. Chen, J. Wang, *J. Mater. Chem. A* **2019**, *7*, 4291.
[44] I. Hussain, G. Tanimu, S. Ahmed, C. U. Aniz, H. Alasiri, K. Alhooshani, *Int. J. Hydrogen Energy* **2023**, *48*, 24663.
[45] M. Al-Hashem, S. Akbar, P. Morris, *Sens. Actuators, B* **2019**, *301*, 126845.
[46] C. J. Heard, J. Čejka, M. Opanasenko, P. Nachtigall, G. Centi, S. Perathoner, *Adv. Mater.* **2019**, *31*, 1801712.
[47] A. M. Ganose, D. O. Scanlon, *J. Mater. Chem. C* **2016**, *4*, 1467.
[48] Y. Du, J. Zhuang, H. Liu, X. Xu, S. Eilers, K. Wu, P. Cheng, J. Zhao, X. Pi, K. W. See, *ACS Nano* **2014**, *8*, 10019.
[49] J. Lu, J. Wu, A. Carvalho, A. Ziletti, H. Liu, J. Tan, Y. Chen, A. C. Neto, B. Ozyilmaz, C. H. Sow, *ACS Nano* **2015**, *9*, 10411.
[50] M. I. Zappia, G. Bianca, S. Bellani, N. Curreli, Z. Sofer, M. Serri, L. Najafi, M. Piccinni, R. Oropesa-Nuñez, P. Marvan, V. Pellegrini, I. Kriegel, M. Prato, A. Cupolillo, F. Bonaccorso, *J. Phys. Chem. C* **2021**, *125*, 11857.
[51] M. I. Zappia, G. Bianca, S. Bellani, N. Curreli, Z. k. Sofer, M. Serri, L. Najafi, M. Piccinni, R. Oropesa-Nuñez, P. Marvan, *J. Phys. Chem. C* **2021**, *125*, 11857.
[52] H. Hahn, G. Frank, *Z. Anorg. Allg. Chem.* **1955**, *278*, 340.
[53] G. Micocci, R. Rella, P. Siciliano, A. Tepore, *J. Appl. Phys.* **1990**, *68*, 138.
[54] E. Borisenko, D. Borisenko, I. Bdikin, A. Timonina, B. Singh, N. Kolesnikov, *Mater. Sci. Eng., A* **2019**, *757*, 101.
[55] H. d'Amour, W. B. Holzapfel, A. Polian, A. Chevy, *Solid State Commun.* **1982**, *44*, 853.
[56] G. Arancia, M. Grandolfo, C. Manfredotti, A. Rizzo, *Phys. Status Solidi A* **1976**, *33*, 563.
[57] A. Kuhn, A. Bourdon, J. Rigoult, A. Rimsky, *Phys. Rev. B* **1982**, *25*, 4081.
[58] A. Kuhn, A. Chevy, R. Chevalier, *Acta Crystallogr. B* **1976**, *32*, 983.
[59] C. De Blasi, D. Manno, A. Rizzo, *Il Nuovo Cimento D* **1989**, *11*, 1145.
[60] A. R. Barron, *Adv. Mater. Opt. Electron.* **1995**, *5*, 245.
[61] J. Brebner, *J. Phys. Chem. Solids* **1964**, *25*, 1427.
[62] E. Aulich, J. L. Brebner, E. Mooser, *Physica Status Solidi.* **1969**, *31*, 129.
[63] J. C. J. M. Terhell, R. M. A. Lieth, *Phys. Status Solidi A* **1971**, *5*, 719.
[64] H. Gerischer, *J. Electroanal. Chem. Interfac.* **1983**, *150*, 553.
[65] V. Fung, G. Hu, P. Ganesh, B. G. Sumpter, *Nat. Commun.* **2021**, *12*, 88.
[66] Y. Shi, T. Liu, R. Hu, H. Xu, C. Yang, L. Yang, L. Feng, X. Jiang, *J. Mater. Chem. A* **2024**, *12*, 4770.
[67] M. M. Monshi, S. M. Aghaei, I. Calizo, *Surf. Sci.* **2017**, *665*, 96.
[68] A. Harvey, C. Backes, Z. Gholamvand, D. Hanlon, D. McAteer, H. C. Nerl, E. McGuire, A. Seral-Ascaso, Q. M. Ramasse, N. McEvoy, *Chem. Mater.* **2015**, *27*, 3483.
[69] C. J. Powell, A. Jablonski, *Nucl. Instrum. Methods Phys. Res., Sect. A* **2009**, *601*, 54.
[70] D. W. Boukhvalov, V. Paolucci, G. D'Olimpio, C. Cantalini, A. Politano, *Phys. Chem. Chem. Phys.* **2021**, *23*, 7541.
[71] M. P. Kiskinova, *Poisoning and promotion in catalysis based on surface science concepts and experiments*, Elsevier, Amsterdam, **1991**.
[72] M. Batzill, U. Diebold, *Phys. Chem. Chem. Phys.* **2007**, *9*, 2307.
[73] D. Degler, S. A. Müller, D. E. Doronkin, D. Wang, J.-D. Grunwaldt, U. Weimar, N. Barsan, *J. Mater. Chem. A* **2018**, *6*, 2034.
[74] G. D'Olimpio, S. Nappini, M. Vorokhta, L. Lozzi, F. Genuzio, T. O. Mentes, V. Paolucci, B. Gurbulak, S. Duman, L. Ottaviano, A. Locatelli, F. Bondino, D. W. Boukhvalov, A. Politano, *Adv. Funct. Mater.* **2020**, *30*, 2005466.
[75] O. A. Balitskii, V. P. Savchyn, P. V. Savchyn, *Physica B* **2005**, *355*, 365.
[76] M.-A. Ha, R. E. Larsen, *J. Electrochem. Soc.* **2021**, *168*, 024506.
[77] A. Zagalskaya, V. Alexandrov, *J. Phys. Chem. Lett.* **2020**, *11*, 2695.
[78] F. Opoku, O. Akoto, N. K. Asare-Donkor, A. A. Adimado, *Appl. Surf. Sci.* **2021**, *562*, 150188.
[79] S. Jung, S. Jang, K. H. Baik, in *Gallium Oxcide*, (Eds: S. Pearton, F. Ren, M. Mastro), Elsevier, Amsterdam, **2019**, p. 439.
[80] H. Zhai, Z. Wu, Z. Fang, *Ceram. Int.* **2022**, *48*, 24213.
[81] J. Zhu, Z. Xu, S. Ha, D. Li, K. Zhang, H. Zhang, J. Feng, *Materials* **2022**, *15*, 7339.
[82] U. Hoefer, J. Frank, M. Fleischer, *Sens. Actuators, B* **2001**, *78*, 6.
[83] J. Szlachetko, J. Szade, E. Beyer, W. Błachucki, P. Ciochoń, P. Dumas, K. Freindl, G. Gazdowicz, S. Glatt, K. Guła, J. Hormes, P. Indyka, A. Klonecka, J. Kołodziej, T. Kołodziej, J. Korecki, P. Korecki, F. Kosiorowski, K. Kosowska, G. Kowalski, M. Kozak, P. Kozioł, W. Kwiatek, D. Liberda, H. Lichtenberg, E. Madej, A. Mandziak, A.

Marendziak, K. Matlak, A. Maximenko, et al., *Eur. Phy. J. Plus.* **2023**, *138*, 10.

[84] P. Giannozzi, S. Baroni, N. Bonini, M. Calandra, R. Car, C. Cavazzoni, D. Ceresoli, G. L. Chiarotti, M. Cococcioni, I. Dabo, A. Dal Corso, S. de Gironcoli, S. Fabris, G. Fratesi, R. Gebauer, U. Gerstmann, C. Gougoussis, A. Kokalj, M. Lazzeri, L. Martin-Samos, N. Marzari, F. Mauri, R. Mazzarello, S. Paolini, A. Pasquarello, L. Paulatto, C. Sbraccia, S. Scandolo, G. Sclauzero, A. P. Seitsonen, et al., *J Phys Condens Matter* **2009**, *21*, 395502.

[85] J. P. Perdew, K. Burke, M. Ernzerhof, *Phys. Rev. Lett.* **1996**, *77*, 3865.

[86] V. Barone, M. Casarin, D. Forrer, M. Pavone, M. Sambi, A. Vittadini, *J. Comput. Chem.* **2009**, *30*, 934.

[87] D. Vanderbilt, *Phys. Rev. B* **1990**, *41*, 7892.